

Proton-induced halo formation in charged meteors*

Ante Šiljić,^{1,2} Frane Lunić,¹ Jurica Teklić,¹ Dejan Vinković^{1,3,4,†}

¹Faculty of Science, University of Split, Rudjera Boškovića 33, HR-21000 Split, Croatia,

²Ericsson Nikola Tesla d.d., Poljička cesta 39, HR-21000 Split, Croatia

³Science and Society Synergy Institute, Bana Josipa Jelačića 22, HR-40000 Čakovec, Croatia

⁴HiperSfera d.o.o., Ilica 36, HR-10000 Zagreb, Croatia

[†]To whom correspondence should be addressed; E-mail: dejan@iszd.hr.

Estimates of the daily mass input of interplanetary dust particles into the Earth's atmosphere range from 5 to 300 tonnes per day (*I*). The ablation of those meteoroid particles, as they enter the atmosphere at hypersonic speeds between ~ 10 km/s and 72 km/s, is manifested as meteors. Despite a very long history of meteor science, our understanding of meteor ablation and its shocked plasma physics is still far from satisfactory as we are still missing the microphysics of meteor shock formation and its plasma dynamics. Here we argue that electrons and ions in the meteor plasma undergo spatial separation due to electrons being trapped by gyration in the Earth's magnetic field, while the ions are carried by the meteor as their dynamics is dictated by collisions. This separation process charges the meteor and creates a strong local electric field. We show how acceleration of protons in this field leads to the collisional excitation of ionospheric N_2 on the scale of many 100 m. This mechanism ex-

*The initial version of this manuscript was submitted to Nature Astronomy on August 1, 2016, a revised version submitted on January 3, 2017, and finally rejected on March 15, 2017. It is currently under revision for submission to another journal.

plains the puzzling large halo detected around a Leonid meteor (2), while it also fits into the theoretical expectations of several other unexplained meteor related phenomena. We expect our work to lead to more advanced models of meteor-ionosphere interaction, combined with the electrodynamics of meteor trail evolution (3, 4).

The physics of meteor-atmosphere interaction is powered by the high level of kinetic energy of meteors, with the light production from collisionally excited atoms as the visually most prominent process. From the public policy point of view, large meteors with enough kinetic energy to penetrate deep into the atmosphere and produce ground damage are of the most concern, as recently seen in the case of Chelyabinsk meteor (5). The Chelyabinsk event stirred up the interest for meteor physics, but the need for better understanding of meteor plasma physics has been already growing in recent years as new meteor related phenomena were discovered. Detection of meteors above typical 130 km altitude was explained by thermalization of sputtered particles (6, 7), but the theoretical model does not go beyond basic physical principles. Radar observations of such high-altitude meteors indicate the importance of magnetic field and suggest the existence of new types of high-altitude meteors that are possibly a result of some electrodynamic instability triggered by a meteor (8). Electrodynamic coupling between meteors and ionosphere was also invoked as a possible explanation for the phenomenon of anomalous meteor sounds (electrophones, see (9)), based on their instrumental detection (10).

Another phenomenon, still not explained beyond simple narratives, is large scale (up to ~ 2 km) jet-like features emanating from high-speed meteors at altitudes above 100 km (11). Fragmentation is a preferred explanation for this and many other unusual meteor light properties, but the cases of high separation speeds of fragments at altitudes too high for fragmentation (13) and fast (millisecond) high-amplitude flickering of light curves (12) are beyond this simple explanation. Instead, electrical forces due to accumulated charge in the meteoroid body are

sought to explain these phenomena (*12, 13*). This would also agree with the radar observations of oscillating meteor plasma (*14*) and the phenomenon of meteors triggering sprites (large-scale electrical discharges high above thunderstorms) by creating kilometer-size plasma irregularities in the ionosphere (*15*). Such a large irregularity has been detected in a form of a kilometer sized halo around a Leonid meteor in 2001 at altitudes between 104 km and 110 km (*2*). This is a surprising discovery because the size of a meteor plasma ball can be of the order of 1 m, as shown by scattering of radar waves (see section S2 in Supplementary Information), since the atmospheric mean free path at 105 km altitude is ~ 0.33 m. A similar halo effect was detected again in 2002 Leonids (*16*), but not as bright as in the case of 2001 Leonid. The authors in (*2*) considered precursor UV photoionization as a possible source of the halo but dismissed it as inefficient.

All these phenomena indicate that meteor plasma produces electromagnetic effects on distances larger than what can be reached by thermal collisions of hot meteor plasma. We are reviving an old idea of electrically charged meteors that has been so far controversial due to a weak theoretical and observational support (except for micrometeoroids (*17*), which are not the topic of our study). The weakly ionized meteor plasma under hypersonic shock conditions produces a self-induced electric field (*18*), but the net charge of the meteor is considered neutral. In Supplementary Information (section S5.1) we give a short overview of existing research on meteor charging, with experiments indicating charge separation at hypersonic speeds. However, the influence of the Earth's magnetic field on the charge dynamics in the meteor head (the immediate surrounding of a meteoroid that includes the shocked region) has not been investigated in any detail. Interestingly enough, in (*2*) the authors speculate that "interaction of the ionized particles with the Earth's magnetic field will cause charge separation that can set up strong local electric fields", which in turn would feed plasma instabilities, but dismiss this idea because ions have a small ($\lesssim 1$ m) mean free path at these altitudes. We show how charge separation still can

happen and how accelerated protons can travel long enough distances for the halo to emerge.

Meteors ablate mostly in the dynamo layer of the ionosphere between 75 km and 125 km altitude where the electron collision frequency is lower than the electron cyclotron frequency, but the ion collision frequency is still larger than the ion cyclotron frequency. Ions are therefore largely coupled to the neutral gas while electrons are largely decoupled (19). When meteors move with an angle to the Earth's magnetic field, electrons in the meteor plasma may stay trapped by the magnetic field while ions keep traveling with the meteor. We argue that this facilitates charge accumulation on meteors. The net charge creates an electric field, which can accelerate charged particles that collide with the atmospheric molecules.

This process is the most efficient in the meteor plasma with the highest speed relative to the magnetic field, which is the region of diffuse shock layer. The formation of diffuse shock is enhanced by the intense meteoroid evaporation, which creates a vapor cloud around the body at altitudes of low atmospheric density where the shock front would not form (20). The side-lobes of the diffuse bow shock layer are the most susceptible to the leakage of magnetized electrons, since this flow of electrons cannot be stopped by the stagnation zone in front of the meteoroid body (21).

We explore this process at 105 km altitude for Leonid meteors with the velocity of $v_m = 71$ km/s, where the meteor halo and some other phenomena present a challenge to the meteor physics. The charge separation can be only partially successful because an electric field builds up along the line of charge separation and drives a neutralization current. The magnetic field is largely unperturbed since the magnetic Reynolds number stays below one (section S1 in Supplementary Information; notice how this condition breaks down at lower altitudes). Hence, the mobility of electrons dictates the strength of the current that tries to balance the charges. The electron conductivity σ_e^m is anisotropic and it depends on the direction of magnetic and electric field. We are interested in the conductivity along the electric field lines that drive the

neutralization current. In the case when the angle between the meteor flight and the Earth's magnetic field \vec{B} is close to perpendicular, we use the Pedersen conductivity within the meteor plasma $\sigma_e^m = \sigma_0^m \nu_e^2 / (\nu_e^2 + \omega_{ce}^2)$, where σ_0^m is the plasma conductivity, $\omega_{ce} = 10^7$ Hz is the cyclotron frequency of electrons and ν_e is the electron-neutral collision frequency. When $\nu_e > \omega_{ce}$ or the meteor flight is parallel to \vec{B} , the conductivity becomes $\sigma_e^m = \sigma_0^m$.

The charge conservation gives the balance equation $\sigma_e^m E_m = n_e^m e v_m$, where E_m is the electric field (in units of V/m), n_e^m is the number density of electrons in meteor plasma (in units of m^{-3}) and e is the electron charge. The relative speed between charges during separation is approximately v_m , which is much larger than thermal speeds. We use $\sigma_0^m = n_e^m e^2 / m_e \nu_e$, where m_e is the electron mass, and derive:

$$E_m \sim \begin{cases} 4 \times 10^{-7} \nu_e & \text{if } (\nu_e > \omega_{ce} \text{ and } \vec{v}_m \perp \vec{B}) \text{ or } \vec{v}_m \parallel \vec{B} \\ 4 \times 10^7 / \nu_e & \text{if } (\nu_e < \omega_{ce} \text{ and } \vec{v}_m \perp \vec{B}) \end{cases} \quad (1)$$

We see that for $\vec{v}_m \perp \vec{B}$ the electric field has at least a few V/m and can reach higher values as ν_e deviates from $\omega_{ce} = 10^7$ Hz. We do not exclude a possibility that the electric field might be also boosted by the internal trail currents induced by the external electric fields (3). Notice also that the constants are derived using $v_m = 71$ km/s, while a more general approach would yield a linear dependence of E_m on v_m .

The collision frequency can be estimated from its basic definition as $\nu_e = n_m Q_e \langle v \rangle$, where n_m is the number density of neutrals in the meteor plasma, Q_e is the collisional cross section and $\langle v \rangle = 6 \times 10^3 \sqrt{T_e}$ is the average thermal speed of electrons (in units of m/s) of temperature T_e (in Kelvins). The measured equilibrium temperatures in meteor plasma remain in a narrow range around $\sim 4,500$ K for a wide range of entry speed and initial mass (22). The electrons in meteor plasma collide mostly with atomic species, with $Q_e \sim 5 \text{ \AA}^2$ as an approximate average collisional cross section (at ~ 1 eV; e.g. see (23)). The plasma density can be estimated by comparing dynamics pressure of incoming air and the thermal pressure of compressed meteoroid

plasma $\eta m_{atm} n_{atm} v_m^2 / 2 = n_m k T_m$, where m_{atm} is the average atmospheric molecular mass and n_{atm} is the atmosphere number density. The plasma temperature is assumed in equilibrium as $T_m = T_e$. The dimensionless constant $\eta < 1$ is introduced to accommodate for a fast drop in pressure outside the stagnation zone, as seen in numerical simulations (21, 24).

Conditions at 105 km altitude are $m_{atm} = 4.6 \times 10^{-26}$ kg and $n_{atm} = 4.4 \times 10^{18}$ m⁻³, which gives $n_m = \eta \times 10^{22}$ m⁻³. This agrees well with the range of densities in numerically simulated meteors (24), which show $\eta < 10^{-2}$ in the relaxation zone on the sides and behind the meteoroid (21, 24). Using these values we derive the collision frequency $\nu_e = 2\eta \times 10^8$ Hz. The above estimate on η gives $\nu_e < \omega_{ce}$ and the angle between \vec{v}_m and \vec{B} becomes the critical parameter in deriving the strength of electric field E_m . A case with $\vec{v}_m \parallel \vec{B}$ would yield small electrical fields, but the field could reach tens or hundreds of V/m when the meteor flight is close to $\vec{v}_m \perp \vec{B}$.

Accumulated net charge in the meteor head powers some secondary effects that can be detected from the ground. Strong electrostatic repulsion between fragments of a fractured meteoroid can result in meteor fragmentation with high relative speeds between fragments. Such a high-speed fragmentation has been detected and in Supplementary Information (section S2) we show how our model is in agreement with the required amount of accumulated charge (13). Meteor fragmentation is monitored lately using high-power, large-aperture VHF/UHF radar systems that can detect the meteor head-echo - the radar reflection from the plasma surrounding the meteoroid in the meteor head. Interestingly, some radar signals can be explained only with a model of pulsating size of the meteor head plasma (14). Meteor pulsation, possibly due to meteor charging, has been also invoked to explain millisecond flares in the light curves of fireballs (12). In Supplementary Information (section S3) we show how meteor charging in our model inevitably leads to oscillations of the net charge of meteor head plasma, which explains the observed pulsating phenomena.

The net charge accumulated in the meteor head would also produce an electric field around the meteor. The surrounding weakly ionized ionosphere reacts to the electric field by driving electric currents. Strong enough currents might induce collisionally excited emission from the neutral atmospheric species, which would explain a large glowing halo detected around a Leonid meteor (2). However, we find this process unlikely since these currents are dominantly due to ionospheric electrons, as they are more mobile than ions, but the electrons are magnetized and accelerate along the magnetic field lines, which prevents them from creating a halo-like structure,

A strong electric field would also eject ions out of the meteor head. Ions are heavy compared to electrons and cannot reach high speeds under these conditions, except in the case of protons. Protons change into hydrogen atoms and back through the collisional process of charge exchange and electron stripping. The presence of hydrogen in bright meteors, including Leonids, has been revealed through hydrogen emission lines (25, 26). Hydrogen is a product of the meteoroid ablation and it belongs to the "hot" component of a meteor spectrum, which seems to be related to the impact excitation during non-thermal collisions with the atmosphere. This implies that hydrogen is excited within the diffuse shock and, in our case, in the meteor halo. This also agrees with the observation that the intensity of the high-excitation hydrogen emission follows atmospheric nitrogen, not the meteor afterglow (25).

The first positive band of N_2 ($B^3\Pi_g-A^3\Sigma_u^+$) is the most probable source of the meteor halo emission caused by proton/H collisions with the atmospheric N_2 : i) it is regularly detected in meteor spectra (25–28), ii) its wavelength range fits the spectral range of the camera ($\sim 700 \pm 200 \mu m$) that imaged the halo (2, 29), and iii) it has short enough radiative lifetimes (29) to emit within the high-speed camera frame length of 1 ms (otherwise the imaged halo would be elongated). The plasma temperature responsible for N_2 emission is not easily constrained - derived temperatures vary from ~ 4500 K (22) to ~ 8000 K (26). The reason might be in

the contribution to emission from non-equilibrium excitations of N_2 during fast one-directional collisions in the diffuse shock, and possibly in halo. Various ratios of equilibrium to non-equilibrium emission would lead to different temperature estimates, which can manifest itself as a bi-modal temperature of meteor plasma with the main spectrum indicating ~ 4000 K and the second spectrum, probably originating from the shock, showing $\sim 10\,000$ K (30).

Using these assumptions, we performed a numerical simulation of proton/H transport through the ionosphere under the influence of meteor electric field. The goal is to reconstruct the brightness profile of the imaged halo around a Leonid meteor (2) at 105 km altitude. The simulation is based on proton aurora models (31) tracing ionization, excitations, charge exchange and electron stripping processes on N_2 , O_2 and O (section S5.2 in Supplementary Information). A simulation particle is traced until its energy drops below a threshold value or its distance from the meteoroid becomes too large. The details of the simulation algorithm are available in Supplementary Information (section S5).

Our attempts to reconstruct the halo image by ejecting protons into various solid angles positioned along the direction of meteor flight resulted in an interesting conclusion that ejection angles should prefer backward directions (see figure S2 in Supplementary Information). The reason for this angle exclusion mechanism is the small viewing angle of about 30° between the camera direction and the meteor line of flight, which makes axially-symmetric halo structures appear very symmetric and positioned too far ahead of the meteoroid. The solution was to eject protons mainly into backward directions. The search of the best fit to the brightness profile yielded a choice where protons are ejected into directions between $\vartheta_0 = 60^\circ$ and $\vartheta_1 = 150^\circ$ relative to the direction of meteor flight, with a probability $\vartheta_0 - (\vartheta_0 - \vartheta_1)\sqrt{\mathfrak{R}}$, where \mathfrak{R} is a random number. These angles should be considered only as a rough approximation since we are dealing with an approximate model of the meteor head plasma configuration and ionospheric electric field geometry and screening (with no better option, we use an ad hoc point charge

geometry and a power law charge screening).

It is interesting to note that a numerical simulation of radiative gasdynamic model of physically and chemically nonequilibrium flow around ablating meteoroid yields enhanced hydrogen production predominantly in the backward sidelobes relative to the meteoroid (21). This is in agreement with our constraint on ejection angles and with the expectation that the flow momentum will carry plasma atoms out of the back and sides of the meteor head.

The result of our halo simulation is shown in Fig. 1 from two viewpoints - the camera that detected the halo around a Leonid meteor and the sideview that provides a better insight into the halo structure. The meteor itself is not shown, but the arrow marks the position of the meteor head and meteor trail. The image reconstructs the size of the detected halo. The brightness profile of the halo perpendicular to the meteoroid velocity vector is shown in Supplementary Information (section S5.3) and compared with the observed brightness profile. We also present results from a model that simulates propagation of UV photons (figures S5 and S6). We confirm that UV cannot explain the halo, although this does not exclude a possibility that UV shock precursor photons are emitted and absorbed by the immediate meteor head surroundings.

The existence of a kilometre-scale halo caused by a corona discharge from a charged meteor had been speculated already in the 60's (32), but weak theoretical arguments and the lack of convicting observational confirmation of charged meteors had kept this phenomenon on the fringe of meteor astronomy. Our model of charged meteor plasma infers that detected meteor halo (2, 16), oscillations of meteor head plasma (14), and fragmentation of meteoroids that result in large transverse speeds (13) are all manifestations of charged meteors. Moreover, the spatial size of produced ionospheric irregularity of enhanced ionization is such that it is maybe a trigger of various other phenomena. For example, the first instrumental detection of electrophonic sounds performed during 1998 Leonid meteor storm (10) pointed to the existence of a larger ionospheric disturbance triggered by meteors. Also, a kilometer-scale plasma irregularities at

about 90 km altitude are identified recently as precursors of sprite streamer initiation, with meteors as possible origin of these irregularities (15).

Phenomena like fast jet-like features from meteors (11, 12) might also be related to strong local electric fields. In jets from high-altitude meteors (above ~ 130 km, (33)) the magnetic and electric fields must play an important role as the meteor plasma is of a low density while both electrons and ions are magnetized. Also, the role of possible trail currents (3) in enhancing the meteor head electric field is not explored in detail. This and other processes could boost the meteor head charging. For example, the magnetic Reynolds number (section S1 in Supplementary Information) indicates that below 100 km altitude the magnetic field might become compressed in front of the meteoroid (stagnation zone), which would result in ambipolar diffusion of electrons. The incoming flow would extract those electrons and enhance the process of meteor head charging. In general, we need to explore meteor plasma microphysics in much more detail, with external magnetic and electric fields included, while concurrently put more effort into observations of various poorly understood meteor related phenomena.

References

1. Plane, J.M.C. Cosmic dust in the earth's atmosphere. *Chem. Soc. Rev.* **41**, 6507-6518 (2012).
2. Stenbaek-Nielsen, H.C. & Jenniskens, P. A "shocking" Leonid meteor at 1000 fps. *Adv. Space Res.* **33**, 1459-1465 (2004).
3. Dimant, Y.S., Oppenheim, M.M. & Milikh, G.M. Meteor plasma trails: effects of external electric field. *Ann. Geophys.* **27**, 279-296 (2009).
4. Oppenheim, M.M. & Dimant, Y.S. First 3-D simulations of meteor plasma dynamics and turbulence. *Geophys. Res. Lett.* **42**, 681-687 (2015).

5. Popova, O.P., et al. Chelyabinsk Airburst, Damage Assessment, Meteorite Recovery, and Characterization. *Science* **342**, 1069-1073 (2013).
6. Vinković, D. Thermalization of sputtered particles as the source of diffuse radiation from high altitude meteors. *Adv. Space Res.* **39**, 574-582 (2007).
7. Popova, O.O., Strelkov, A.S. & Sidneva, S.N. Sputtering of fast meteoroids' surface. *Adv. Space Res.* **39**, 567-573 (2007).
8. Gao, B. & Mathews, J.D. High-altitude meteors and meteoroid fragmentation observed at the Jicamarca Radio Observatory *Mon. Not. R. Astron. Soc.* **446**, 3404-3415 (2015).
9. Lamar D.L. & Romig, M.F. Anomalous Sounds and Electromagnetic Effects Associated with Fireball Entry. *Meteoritics*, **2**, 127-136 (1964).
10. Zgrablić, G., et al. Instrumental recording of electrophonic sounds from Leonid fireballs. *J. Geophys. Res.* **107**, 1124 (2002).
11. LeBlanc, A.G., et al. Evidence for transverse spread in Leonid meteors. *Mon. Not. R. Astron. Soc.* **313**, L9-L13 (2000).
12. Spurný, P. & Ceplecha, Z. Is electric charge separation the main process for kinetic energy transformation into the meteor phenomenon? *Astron. Astrophys.* **489**, 449-454 (2008).
13. Stokan, E. & Campbell-Brown, M.D. Transverse motion of fragmenting faint meteors observed with the Canadian Automated Meteor Observatory. *Icarus* **232**, 1-12 (2014).
14. Kero, J., et al. Three-dimensional radar observation of a submillimeter meteoroid fragmentation. *Geophys. Res. Lett.* **35**, L04101 (2008).

15. Qin, J., Pasko, V.P., McHarg, M.G. & Stenbaek-Nielsen, H.C. Plasma irregularities in the D-region ionosphere in association with sprite streamer initiation. *Nature Comm.* **5**, id.3740 (2014).
16. Jenniskens, P., The 2002 Leonid MAC Airborne Mission: First Results. *WGN* **30**, 218-224 (2002).
17. Mendis, D.A., Wong, W.-H., Rosenberg, M. & Sorasio, G. Micrometeoroid flight in the upper atmosphere: Electron emission and charging. *J. Atmos. Solar Terr. Phys.* **67**, 1178-1189 (2005).
18. Farbar, E.D. & Boyd, I.D. Modeling of the plasma generated in a rarefied hypersonic shock layer. *Phys. Fluids*, **22**, 106101-12 (2010).
19. Schunk, R.W. & Nagy, A.F. *Ionospheres: Physics, Plasma Physics, and Chemistry*, Cambridge University Press (2000).
20. Popova, O.P., Sidneva, S.N., Shuvalov, V.V. & Strelkov, A.S. Screening of Meteoroids by Ablation Vapor in High-Velocity Meteors. *Earth Moon Planets* **82/83**, 109-128 (2000).
21. Surzhikov, S.T. Non-Equilibrium Radiative Gas Dynamics of Small Meteor. *44th AIAA Fluid Dynamics Conference*, AIAA Aviation (AIAA 2014-2636) (2014).
22. Jenniskens, P., Laux, C.O., Wilson, M.A. & Schaller, E.L. The Mass and Speed Dependence of Meteor Air Plasma Temperatures. *Astrobiology* **4**, 81-94 (2004).
23. Itikawa, Y. & Ichimura, A. Cross Sections for Collisions of Electrons and Photons with Atomic Oxygen. *J. Phys. Chem. Ref. Data* **19**, 637-651 (1990).
24. Boyd, I.D. Computation of Atmospheric Entry Flow about a Leonid Meteoroid. *Earth Moon Planets* **82/83**, 93-108 (2000).

25. Jenniskens, P. & Mandell, A.M. Hydrogen Emission in Meteors as a Potential Marker for the Exogenous Delivery of Organics and Water. *Astrobiology* **4**, 123-134 (2004).
26. Kasuga, T., Iijima, T. & Watanabe, J. Is a 2004 Leonid meteor spectrum captured in a 182cm telescope? *Astron. Astrophys.* **474**, 639-645 (2007).
27. Jehin, E., et al. Spectroscopic anatomy of a meteor with the very large telescope (ESO). *Adv. Space Res.* **39**, 550-554 (2007).
28. Borovička, J., Stork, R. & Bocek, J. First results from video spectroscopy of 1998 Leonid meteors. *Meteorit. Planet. Sci.* **34**, 987-994 (1999).
29. Forrest, R.G., Russ, R.L. & Patrick, J.E. Franck-Condon Factors, r-Centroids, Electronic Transition Moments, and Einstein Coefficients for Many Nitrogen and Oxygen Band Systems. *J. Phys. Chem. Ref. Data* **21**, 1005-1107 (1992).
30. Borovička, J. Two components in meteor spectra. *Planet. Space Sci.* **42**, 145-150 (1994).
31. Solomon, S.C. Auroral particle transport using Monte Carlo and hybrid methods. *J. Geophys. Res.* **106**, 107-116 (2001).
32. Dokuchayev, V.P. Electrical Discharge During the Flight of Meteors in the Earth's Atmosphere. *Dokl. Akad. Nauk SSSR* **131**, 78-81 (1960).
33. Spurný, P., et al. New type of radiation of bright Leonid meteors above 130 km. *Meteorit. Planet. Sci.* **35**, 1109-1115 (2000).
34. Close, S., Oppenheim, M., Hunt, S. & Coster, A. A technique for calculating meteor plasma density and meteoroid mass from radar head echo scattering. *Icarus* **168**, 43-52 (2004).

35. Marshall, R.A. & Close, S. An FDTD model of scattering from meteor head plasma. *J. Geophys. Res.* **120**, 5931-5942 (2015).
36. Hedin, A.E. Extension of the MSIS thermosphere model into the middle and lower atmosphere. *J. Geophys. Res.* **96**, 1159-1172 (1991).
37. Basu, B., et al., Linear Transport Theory of Auroral Proton Precipitation: A Comparison With Observations. *J. Geophys. Res.* **92**, 5920-5932 (1987).
38. Rees, M.H. *Physics and chemistry of the upper atmosphere*, Cambridge University Press (1989).
39. Basu, B., et al. Transport-Theoretic Model for the Electron-Hydrogen Atom Aurora 1. Theory. *J. Geophys. Res.* **98**, 21517-21532 (1993).
40. Beech, M. & Foschini, L. A space charge model for electrophonic bursters. *Astron. Astrophys.* **345**, L27-L31 (1999).
41. Thébault, E., et al. International Geomagnetic Reference Field: the 12th generation. *Earth, Planets, and Space* **67**, id.#79 (2015).
42. Jenniskens, P. Meteor induced chemistry, ablation products, and dust in the middle and upper atmosphere from optical spectroscopy of meteors. *Adv. Space Res.* **33**, 1444-1454 (2004).
43. ter Haseborg, J. L. & Trinks, H. Electric Charging and Discharging Processes of Moving Projectiles. *IEEE Transactions on Aerospace and Electronic Systems* **AES-16**, 227-232 (1980).
44. ter Haseborg, J. L. & Trinks, H. Detection of Projectiles by Electric Field Measurements. *IEEE Transactions on Aerospace and Electronic Systems* **AES-16**, 750-754 (1980).

45. Serov, Yu. L. & Yavor, I.P. Electric charges associated with objects moving at hypersonic velocities. *Soviet Physics. Technical physics.* **36**, 972-975 (1991).
46. Pilyugin, N. N. & Baulin, N. N. Measurement of electric charges formed on bodies and in their wakes during hypersonic motion. *Solar System Research* **27**, 558-573 (1993).
47. Pilyugin, N.N. Measurement of electric charges near bodies under conditions of hypersonic motion. *High Temperature* **32**, 110-121 (1994).
48. Serov, Yu. L. & Yarov, M. P. Waves of charge in an ionized gas ahead of a hypersonic object. *Technical Physics* **41**, 1183-1185 (1996).

Acknowledgments

The work on computational simulations was performed at the Physics Department, University of Split, and included their CPU/GPU cluster, Hybrid, financed by the National Foundation for Science, Higher Education and Technological Development of the Republic of Croatia. The authors also acknowledge the Technology Innovation Centre Međimurje for additional computational resources. D.V. acknowledges membership in the network supported by the COST Action TD1403 Big Data Era in Sky and Earth Observation.

Author Contributions

A.Š. participated in developing the theory and numerical models of electron and proton dynamics, and was involved in science discussion. F.L. participated in developing the numerical model of UV propagation, and was involved in science discussion. J.T. developed fast simulations of proton dynamics capable of running on computer clusters and general purpose GPUs, required for exploration of parameter space. D.V. planned and organized the project, participated in developing the theory and numerical modeling, and wrote the manuscript.

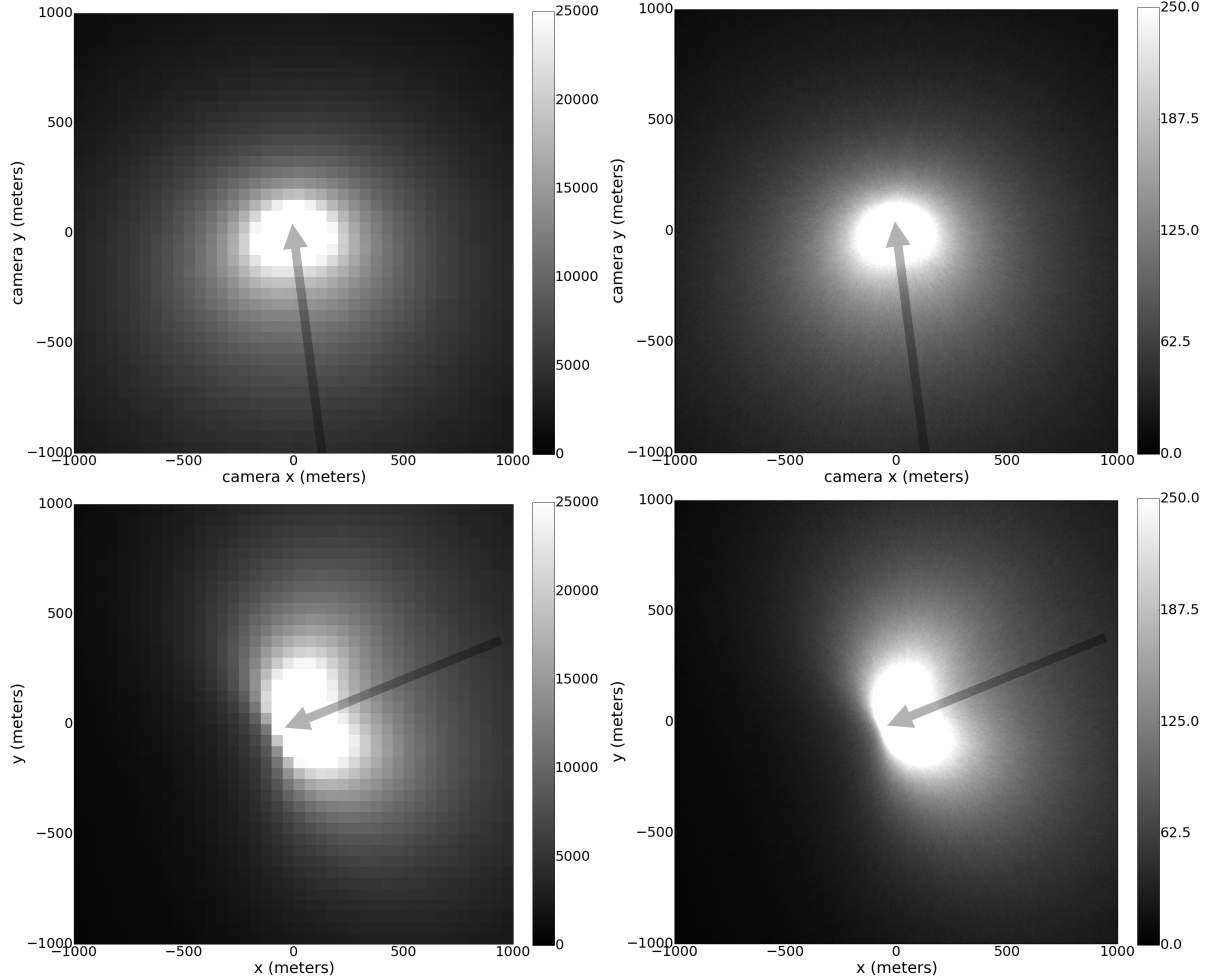


Figure 1: Simulated meteor halo structure at 105 km altitude that was detected around a Leonid meteor (2). The brightness scale is in arbitrary units. Simulation used 10^6 particles ejected from the meteor head. Brightness from the meteor itself is not shown, but gray arrows mark the meteor's position and direction. Images in the upper row show the halo from the view point of the camera that detected the halo, while the lower row shows the halo from a sideview direction perpendicular to the meteor flight trajectory. The left column images have the pixel size similar to the camera and the right column images have a high resolution that shows the halo's fine structure. The emission is a product of proton/hydrogen collisions with the neutral atmosphere, after the protons become ejected from the meteor head due to the meteor's electric field. Details of the simulation process are described in Supplementary Information (section S5).

Supplementary Information

S1. Magnetic Reynolds number in meteor plasma

S2. High speed fragmentation

S3. Meteor head charge oscillation

S4. Electric field screening

S5. Meteor halo modeling

S5.1 Research on charging mechanisms

S5.2 Simulation setup

S5.3 Simulation results

Additional figures

S1 Magnetic Reynolds number in meteor plasma

Magnetic Reynolds number R_m is defined as $R_m = \mu_0 \sigma_0^m L_0 v_0$, where μ_0 is the magnetic permeability, σ_0^m is the plasma conductivity, L_0 is the characteristic length of the meteor and v_0 is the characteristic velocity. The meteor head size in our case is $L_0 \sim 1\text{m}$ and v_0 is the meteor velocity. The conductivity is dominated by elections, which obtain the highest conductivity parallel to the magnetic field $\sigma_0^m = n_e^m e^2 / m_e \nu_e$, where m_e is the electron mass and ν_e is the collision frequency. We already derived $\nu_e = 2\eta \times 10^8 \text{Hz}$ in the main text ($\eta \leq 1$), while measurements indicate the upper meteor electron density of $n_e^m \sim 10^{16} \text{m}^{-3}$ for meteors at 105 km altitude (34). Plugging all these values into the equation for R_m gives $R_m \leq 0.25\eta < 1$. This shows that at these altitudes the magnetic field lines are not frozen into the meteor plasma. However, at altitudes below 100 km the maximum meteor head plasma density increases to $n_e^m \sim 10^{18} \text{m}^{-3}$, which would enable dragging of the magnetic field lines by the meteor plasma in the meteoroid vicinity (where the plasma has its maximum density).

S2 High speed fragmentation

Meteors often fragment during their flight, which can be usually explained by aerodynamic loading. In case of low brightness meteors at altitudes above ~ 80 km, the fragmentation could be due to a non-uniform evaporation of the meteoroid body, with relatively low transverse speeds of fragments. Hence, a detection of high transverse speeds, up to ~ 160 m/s, from low brightness meteors at altitudes of ~ 100 km was a surprise (13). The authors tested several theoretical explanations and concluded that they are inadequate to explain the fragmentation. It is interesting that one of these rejected models was electrostatic repulsion due to a gain of positive charge, but they rejected it because the estimated net charge was on the order of $10^{11}|e|$ (e is the electron charge). We find below that this is not unrealistic and it fits nicely into our theory.

The expected outer boundary of the meteor charge collection is the region of first collisions between the incoming flow and the diffuse shock material. However, the size of the diffuse shock is not well known and its boundary is smoothly connected with the surrounding ionosphere. Scattering of radar waves from the meteor head plasma yielded estimates of the head radius of $r_0 \sim 0.5 - 1$ m (34, 35). For simplicity we will use $r_0 = 1$ m radius. If we assume the basic definition of the electric field $E_m = |e|N_p^0/4\pi\epsilon_0r_0^2$ then the net number of positive charge is $N_p^0 = 7 \times 10^8 E_m$. When E_m is on the level of hundreds of V/m then the accumulated charge N_p^0 reaches the critical values predicted for the anomalously high speeds of transverse motion of fragmenting faint meteors. Since the total number of electrons in meteor head plasma at 105 km is $> 10^{14}$ (34), we see that just a tiny fraction of the electrons in the meteor head needs to be extracted to create strong electric fields.

S3 Meteor head charge oscillation

Fragmentation creates radar signal pulsations due to interference patterns as fragments drift away from each other. This drift can be calculated when observed simultaneously from several radar locations, but a surprise detection was when pulsation signals were simultaneous at all radar stations (*14*). The simplest explanation is an oscillating size of the meteor head plasma. The same phenomenon is implied from the high time resolution light curves of fireballs that exhibit very short, millisecond flares (*12*), which cannot be explained by classical meteor hypersonic flight physics. Instead, the authors evoke meteor charging as a possible explanation, which would lead to periodic discharges that could evaporate a small inner portion of the meteoroid. They speculate that this process can release small fragments into the head plasma, where they evaporate and boost the meteor light production.

In our model of the net charge of the meteor head plasma, the size of the plasma cloud is naturally prone to oscillations. This is a consequence of two balancing processes: one is charge creation and the other is the loss of net charge as the charge moves into the meteor wake or gets ejected by the electrostatic force. The charge production is dominated by the meteor speed and atmosphere density, which do not depend on the meteor net charge, but the charge loss depends on the strength of electrostatic force, which in turn is proportional to the amount of net charge. This creates a feedback loop that powers the charge density oscillations.

The net charge in meteor head is created in collisions of meteor head particles with the incoming atmosphere (source function $S(t)$) and lost when transported into the meteor wake or get ejected into the ionosphere by the electrostatic force (sink function $L(t)$). We can approximate $S(t)$ as a constant within a narrow range of altitudes because the number of collisions is mainly dominated by the meteor speed and atmospheric density. The sink $L(t)$ is more complicated because the loss of net charge is dictated by the electrostatic force proportional to the

amount of accumulated net charge. Hence, $L(t)$ depends on the net charge number density $n_p(t)$ within the meteor head of radius r_0 and on the speed of the leaking charge at the meteor head boundary $v_p(r_0, t)$. We approximate this as $L(t) = \alpha n_p(t) v_p(t)$, where α is a constant for a given r_0 .

In steady state $S = L(t)$, with the charge density and escape velocity at their equilibrium n_p^0 and v_p^0 . Perturbations from the steady state are a consequence of the electric field force removing the positive net charge with an unsteady speed. From the general definition of the force it follows $E_m(r_0, t) \propto dv_p(r_0, t)/dt$, while the definition of electric force gives $E_m(r_0, t) \propto n_p(t)/r_0^p$ (we expect charge screening in plasma, which makes $p < 2$). This yields the escape velocity variations $dv_p(t)/dt = \beta n_p(t)$, where β is a constant for a given r_0 . The charge conservation dictates the balance equation $dn_p(t)/dt = S - L(t)$. If we consider perturbations from the equilibrium speed $v_p(t) = v_p^0 + \delta v(t)$ and from the equilibrium density $n_p(t) = n_p^0 + \delta n_p(t)$ then the charge conservation yields

$$\frac{d\delta n_p(t)}{dt} = -\alpha n_p^0 \delta v(t) - \alpha v_p^0 \delta n_p(t) \quad (2)$$

The same perturbation approach can be applied on the escape velocity variations and obtain

$$\frac{d\delta v_p(t)}{dt} = \beta \delta n_p(t) \quad (3)$$

After combining this equation with the first derivative of the charge conservation, equation 2 yields

$$\frac{d^2 \delta n_p(t)}{dt^2} + \nu \frac{d\delta n_p(t)}{dt} + \omega_0^2 \delta n_p(t) = 0 \quad (4)$$

where $\nu = \alpha v_p^0$ and $\omega_0^2 = \alpha \beta n_p^0$.

This is the classical Damped Harmonic Oscillator equation, with the solution

$$\delta n_p(t) \propto e^{-\nu t/2} \cos(\omega_1 t + \phi) \quad (5)$$

where $\omega_1^2 = \omega_0^2 - \nu^2/4$. The quantitative details are not reachable with this level of approximations, but qualitatively we see that the damping depends on the charge sink rate, while oscillations have a higher frequency for larger electric forces.

S4 Electric field screening

The ionospheric plasma reacts to the positive electric field from a meteor by readjusting the distribution of its charged particles to neutralize the field. We can view this as an accumulation of negative charge closer to the positively charged meteor. We work with a simple point source electric field geometry and homogenous plasma currents. A more realistic electric field is probably not like a point source and the ionospheric currents are influenced by the anisotropic electron mobility. Thus, our description of the screening is an approximation to be used a starting point for exploring the meteor halo structure.

We assume a steady state process of screening, which yields the following steps:

1. A steady state flow of negative charge of density $n_-(r)$ gives $\partial n_-(r)/\partial t = 0$.
2. The charge conservation in spherical geometry is

$$\frac{1}{r^2} \frac{\partial}{\partial r} (r^2 n_-(r) v_-(r)) = 0 \quad (6)$$

where $v_-(r)$ is the ionospheric (average) radial charge velocity during the screening process. This gives $v_-(r) \propto 1/(r^2 n_-(r))$.

3. The radial component of the momentum equation for ionospheric charge dynamics around a meteor gives $eE'(r) = m_e \nu_{en} v_-(r)$, where $E'(r)$ is the electric field around the meteor and ν_{en} is the electron-neutral collision frequency. The collision frequency can be approximated with $\nu_{en} = n_n \sigma_{en} v_-(r)$, where n_n is the density of neutral particles and σ_{en} is the collisional cross section. If we plug this into the momentum equation, and combine it with the step 2

equation for $v_-(r)$, we get

$$E'(r) \propto \frac{1}{r^4 n_-^2(r)} \quad (7)$$

4. The radial component of the gauss law gives

$$\frac{1}{r^2} \frac{\partial}{\partial r} (r^2 E'(r)) \propto n_-(r) \quad (8)$$

5. Now we have to find the electric field that satisfies both steps 3 and 4. Let us assume $E'(r) \propto r^{-p}$. From the step 4 we get $n_-(r) \propto r^{-1-p}$ and from the step 3 $n_-(r) \propto r^{p/2-2}$. These can be satisfied if $p/2 - 2 = -1 - p$, which gives $p = 2/3$.

S5 Meteor halo modeling

S5.1 Research on charging mechanisms

Research on charging of objects flying through air (or other gases), such as aircrafts or fast projectiles, has a very long history (see (43) and references within). In aircrafts this charge can produce various dangerous discharges, while measurements of local electric field disturbances due to accumulated charges on flying projectiles can be used for deducing the projectile velocity and position (44). The research on charging and discharging of supersonic projectiles yielded various results dependent on the projectile properties (size, composition, shape, surface properties, etc.), its speed, and the interaction with the launching platform/gun (43).

Increasing projectile speeds to the hypersonic range, more relevant to the meteor physics, introduces a more challenging physics due to the emergence of plasma flow engulfing the projectile. Laboratory measurements of electric field perturbations by flying projectiles revealed charge separation between the object and its wake, and a formation of a charge precursor in front of the bow shock (45). Photoionization has been invoked as a possible explanation, with charge separation ahead of the body due to the local electric field produced by the charged body and wake. One of the conclusions of this research was that similar phenomena in meteors could

produce large scale ionospheric effects (45). Improved measurements showed that the magnitude of the charge depends on the Mach number M and does not appear until $M > 9$, but the charge polarity depends on various experimental details (46, 47). Further experimental research on the electron precursor revealed that it depends on the instability of waves in the plasma and radiation intensity ahead of the bow shock (48).

While such experiments are indicative of a complicated plasma physics in hypersonic flows, the theory of electrically charged meteors has been so far either over-simplistic (e.g. ignoring details of the meteor plasma physics (32)) or erroneous (e.g. misinterpreting the electric field across the overall electrically neutral shock wave as an external long-distance electric field required or detected on the ground, as well as ignoring that the thermal motion by itself cannot create a significant charge excess on a scale much larger than the Debye length because it lacks energy to overcome the electrostatic forces (40)). A far more promising is a recent theoretical description of induced electric fields in meteor plasma trails by external ionospheric large-scale electric fields (3). Since meteor trails are highly elongated conductors, an expected (albeit not explicitly explored so far) side-effect is a local enhancement of the electric field in the meteor head, where the trail starts, especially in a case of trails oriented more parallel to the magnetic field. The detection of Leonid halo (2), however, happened at the time when conditions were unfavorable for this process as the geomagnetic activity was very low¹ ($K_p \sim 2$) and the shallow East-West meteor direction was oriented more perpendicular to the magnetic and electric field. Nonetheless, it is not excluded that trail currents enhance the electrodynamic effects described in our theory.

¹<http://iswa.ccmc.gsfc.nasa.gov/IswaSystemWebApp/>

S5.2 Simulation setup

The environment in our simulation is set to the conditions defined by the detected Leonid halo (2) at 105 km altitude. The meteor travels with the speed of 71 km/s from the direction of Leonids radiant positioned at the local azimuth of 86.5° (East from North) and elevation of 22° . The camera view direction is 76° (East from North) and 54° elevation. The International Geomagnetic Reference Field model (41) gives the local magnetic field strength of 56,963 nT oriented 24.2° (East from North) and 77.4° Down (the magnetic field components are 12,454 nT horizontal, 11,360 nT North, 5,103 nT East and 55,585 nT Down).

The number densities of atmospheric species at 105 km altitude are taken from the MSISE model of the neutral atmosphere (36): atomic oxygen $n_{atm}(O) = 3.25 \times 10^{17} \text{ m}^{-3}$, molecular oxygen $n_{atm}(O_2) = 7.26 \times 10^{17} \text{ m}^{-3}$ and nitrogen $n_{atm}(N_2) = 3.3 \times 10^{18} \text{ m}^{-3}$. The angle between the magnetic field vector and the meteor line of flight was $\sim 74^\circ$, which is very close to perpendicular and favorable to our theory of the accumulation of net charge. We do not know details of the net charge distribution and the geometry of its electric field, thus we use a simple approximation of a point source. Protons are ejected at distances $r_0 = 1 \text{ m}$ from the meteor center (meteoroid position). The radial strength of electric field at distance r from the meteoroid is $E(r) = E_0/(r/r_0)^p$, where E_0 is the field at r_0 and p is a general form of the power law. We expect deviation from $p = 2$ because of charge screening in the ionosphere. We can only use an approximate derivation of the screening process (see Supplementary Information above), which yields $2 \geq p \geq 2/3$. Both E_0 and p dictate the electric field range of considerable proton acceleration and we can treat them as free parameters. For the canonical model presented here we use $E_0 = 300 \text{ V/m}$ and $p = 2/3$.

Collisional cross section of proton/hydrogen on N_2 , O_2 and O for ionization, excitations, charge exchange and electron stripping processes are taken from (37) and (38) and shown in Figure S1. Elastic collisions of proton/hydrogen atoms display highly forward scattered angles,

hence we approximate it with a pure forward scattering and, therefore, do not have to simulate this process. Inelastic collisions result in energy loss for proton/hydrogen that depends on the collision energy. Average values for these energy losses are taken from Table 1 in (39). We use the screened Rutherford phase function to trace proton/hydrogen atoms after collisions. The scattering azimuthal angle ϑ is obtained from the probability function

$$\cos \vartheta = 1 + 2\epsilon - \frac{2\epsilon(1 + \epsilon)}{1 + \epsilon - \mathfrak{R}} \quad (9)$$

where $\mathfrak{R} \in (0, 1]$ is a random number and

$$\epsilon = \epsilon_0 \frac{1000 \text{ eV}}{E} \quad (10)$$

is a scattering parameter with $\epsilon_0 = 0.001$ and kinetic energy E (in eV) of the proton/hydrogen.

A million protons are ejected at distance $d_0 = 1$ m from the meteoroid into direction \hat{n}_p . This direction is selected relative to the meteor direction, with a random azimuthal angle between 0 and 360° and a random polar angle following the probability function $\vartheta_0 - (\vartheta_0 - \vartheta_1)\sqrt{\mathfrak{R}}$, where \mathfrak{R} is a random number and $\vartheta_0 = 60^\circ$ and $\vartheta_1 = 150^\circ$. We settled with these angles after testing different choices to fit the observed brightness profile. Some examples of model images produced with different choices of ejection polar angles are shown in figure S2.

Within the camera exposure time of $T_{exp} = 0.001$ s the meteor moves with velocity \vec{v}_m away from the position it had at the start of the exposure, which gives the initial proton ejection position $\vec{r}_p = \mathfrak{R} T_{exp} \vec{v}_m + d_0 \hat{n}_p$, where $\mathfrak{R} \in (0, 1]$ is a random number. We set the initial proton velocity equal to \vec{v}_m . The proton is then accelerated by the electric field $E(r)$. The proton switches to hydrogen during charge exchange collisions and hydrogen turns to proton during electron stripping collisions.

For a particle traveling with the speed v_p , the location of its collision is derived from the

time of flight T_{coll} through the atmosphere

$$-\ln \mathfrak{R} = \int_0^{T_{coll}} v_p(t) \sum_i Q_i(v_p) n_{atm}(i) dt \quad (11)$$

where $\mathfrak{R} \in (0, 1]$ is a random number and $i \in \{O, O_2, N_2\}$. The collisional cross section Q_i is the total sum of all cross sections processes for either a proton or a hydrogen atom projectile and it depends on the projectile's kinetic energy, i.e. on v_p . This equation can be solved only by numerical integration, since the particle speed v_p is changing in time due to the influence of electric field. For this purpose we use a simple trapezium rule with the integration time step $\Delta t = 10^{-7}$ s. The collision position is shifted by $-kT_{exp} \vec{v}_m$, where k is the number of exposure times T_{exp} that passed since the start of the exposure. In other words, when the particle flight (including its ejection time $R T_{exp}$) exceeds the exposure time of the camera frame it can be considered as a particle from an older ejection that extended its collisional lifetime into this exposure of our interest.

When a collision happens the collision target is selected randomly from the relative abundances of N_2 , O_2 and O . After that the type of collision (ionization, excitations, charge exchange or electron stripping) is also selected randomly from the relative values of their cross sections. Irrespective of the collision type, we memorize the collision location and assign it the relative value of the nitrogen excitation cross section $Q_{exc}(N_2)/Q_{N_2}$ to speed up the calculation. This is done because our particles are actually statistical representatives of a bunch of particles, where this fraction of them might have participated in the nitrogen excitation. These values are added to the pixels of virtual cameras positioned around the meteor.

A proton quickly reaches 1 keV after ejection and then its path is traced until its energy drops below 1keV or its distance from the meteor exceeds 10 km. Even though some projectiles can still induce nitrogen excitation at these distances, they are spread within such a big volume that their contribution to the image surface brightness becomes negligible. Figure S3 shows an

example of the proton/hydrogen energy at various distances from the meteor. The maximum energy reached in our simulation is about 4keV. The right panel in the figure shows the excitation cross section relevant for photon production. It illustrates the relative importance of different projectile energies in light production.

A sketch of our model is shown in Figure S4, while the pseudocode that describes the overall simulation procedure is as follows:

```

1: Set initial parameters
2: for loop over ejected particles do
3:   Set the initial particle position and velocity
4:   repeat
5:     Set the collision integral value  $I = -\ln R$ 
6:     repeat
7:       Integrate the collision integral in equation 11
8:       Find the electric field
9:       Update particle position and velocity
10:    until the integral becomes equal to  $I$ 
11:    Find  $k$  and shift the collision location
12:    Update camera pixel values for this location
13:    Find the collision type and atmospheric species
14:    Switch between proton and hydrogen if required by the collision type
15:    Find the energy reduction for this collision type
16:    Find new path direction for the particle
17:    Update the particle velocity from the new direction and reduced kinetic energy
18:  until the particle exceeds energy or position limits
19: end for

```

S5.3 Simulation results

The detected halo presented by (2) in their Figure 1 extends hundreds of meters from the meteor head, with a slight brightness even at 1 km distance. On this scale our model manages to keep this level of brightness, as seen in Figure S5. The inner 200 meters around the meteor lack comparison because of pixel saturation in the observed images. There is also observation by (2) in their Figure 6 supposedly showing a structure smaller than 200 meters, but that figure lacks any supporting technical description about the brightness reproduction and pixel size. If we

use the image brightness as *prima facie* grayscale values in the same way as in their Figure 1, and accept the image scale shown in Figure 6 to be correct, then our model can reproduce the brightness profile if $p = 0.4$. However, due to uncertainties with the observed brightness reproduction we do not investigate this in any further detail.

We also show a model of UV propagation in Figure S5 with a simplified favorable assumption that the visible photons from recombination are emitted immediately at the point of absorption of UV photons. Recombination is actually a slow process in the ionospheric plasma and it would create a delay in photon emission, which turns the halo image into a droplet shape, unlike the detected shock-like structure, but for the sake of the argument we ignored this effect. We used absorption cross sections in the 700-750 wavelength range (19), as a typical sample of UV cross sections. The numerical procedure is similar to the proton ejection model, except that photons are absorbed and removed from the simulation at the first interaction with the neutral atmospheric species. We see in Figure S5 that such a UV model cannot explain the halo even with this highly favorable assumption of immediate emission. The UV gets absorbed too quickly in the atmosphere and the brightness falls sharply with the distance, as shown in Figure S6. With this UV simulation we also tested the suggestion that UV photons escape into the atmosphere only within a limited range of azimuthal angles (i.e. backward directions are blocked by the meteor) (42), but Figure S6 shows that this results in a highly symmetric image (because of a small angle between the meteor direction and the line of sight), unlike the observed shock like structure. Notice, however, that we do not exclude the existence of precursor UV photons that would ionize nearby neutral atmosphere, but we show how they do not play a role in the production of a large scale halo around the meteor.

Since our canonical model is based on $E_0 = 300$ V/m and $p = 2/3$, we explore how changes in E_0 and p influence the proton/hydrogen transport and, consequently, the halo image. If we neglect collisions then we can derive the analytic solution for the particle energy (in eV)

from its acceleration $dv/dt = (dv/dr)(dr/dt) = 0.5dv^2/dt$ being equal to the electric force $(|e|E_0/m_p)/(r/r_0)^p$, where m_p is the proton mass. In such a case the solution for the proton/hydrogen energy at distance r from the meteoroid is $E_0(r^{1-p} - r_0^{1-p})/(1-p)$ when $p \neq 1$ and $E_0 \ln(r/r_0)$ when $p = 1$. We see that the energy depends linearly on E_0 , while changes in p from $2/3$ to 1.5 yield energy drop by a factor of ~ 10 . In Figure S7 we show how the particle energy changes with distance when collisions are included. The main trends with E_0 and p remain, but now collisions slow down particles as they move away from the meteoroid. The figure shows that $p = 2/3$ keeps the particle energy almost constant within 1 km distance from the meteoroid, while larger values of p lead to a declining energy with distance. The right panel in Figure S7 shows the nitrogen excitation cross sections, which is equivalent to the relative probability of photon emission. This analysis implies two major consequences on the halo image appearance: reduced E_0 by a factor of 2 leads to lower halo brightness by a factor of ~ 10 , while increased p creates a smaller halo image since particles loose their collision energy with distance faster than in the canonical model. This is then modulated with the sensitivity and resolution of the imaging detector.

Since our model is not an ideal fit to the observations, we tried to deviate from the canonical model. In figure S8 we show how a slight change to the power law from $p=2/3$ to $p=3/4$ improves the fit. And if we allow for experimentation with the proton scattering parameter ϵ then we have a situation like in figure S9 where the fit is improved by keeping ϵ constant. Obviously, there is some degeneracy in the modeling parameters in the way how currently the electric field is configured.

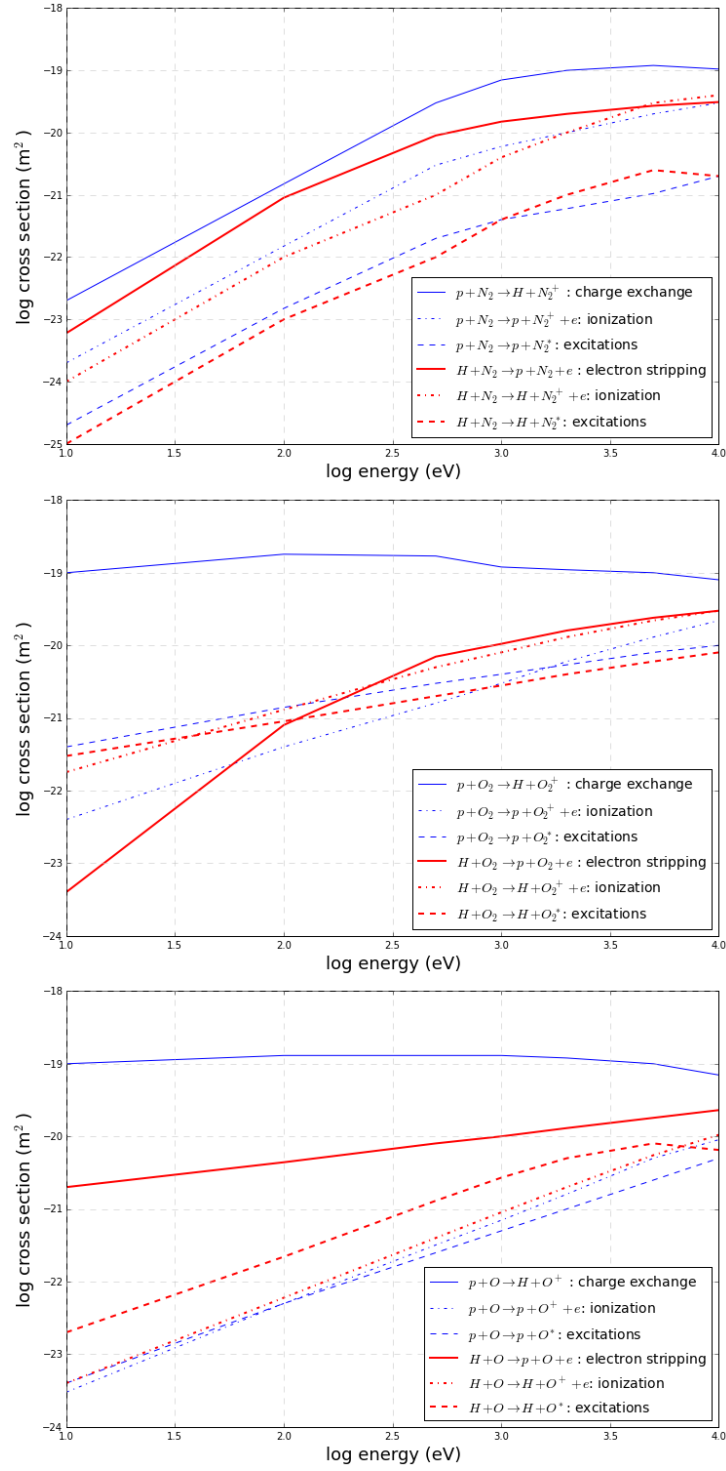


Figure S1: Collisional cross section of proton/hydrogen on N₂, O₂ and O for ionization, excitations, charge exchange and electron stripping processes.

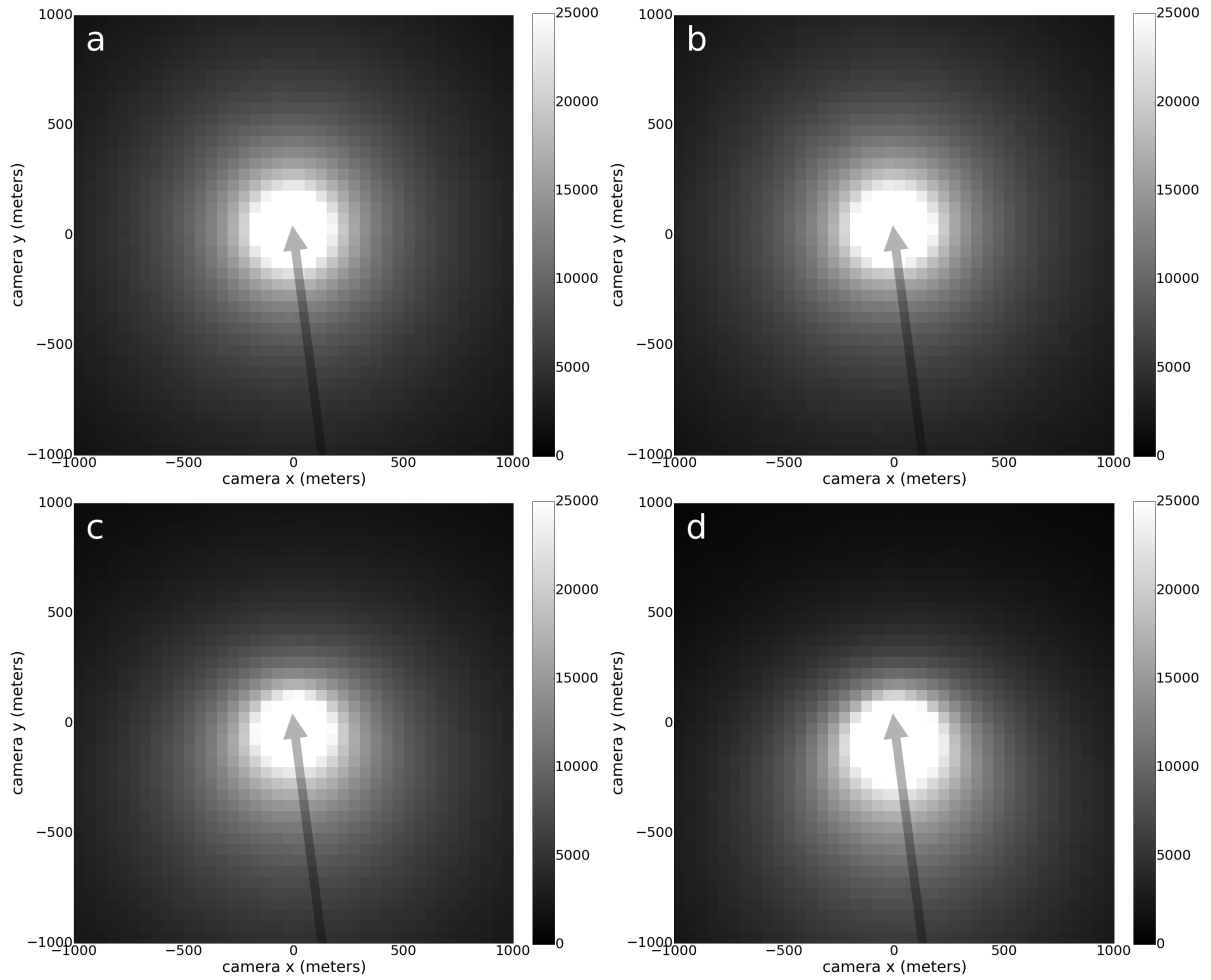


Figure S2: Changes in the range of ejection angles impact the halo shape. These images are produced with proton ejection angles equally distributed between two angles (ϑ_0, ϑ_1). Panels *a* and *b* have $(0^\circ, 180^\circ)$ and $(0^\circ, 160^\circ)$, respectively, while panels *c* and *d* have $(90^\circ, 180^\circ)$ and $(120^\circ, 180^\circ)$, respectively. It is evident that matching model images to the observed halo requires an emphasis on backward ejection angles.

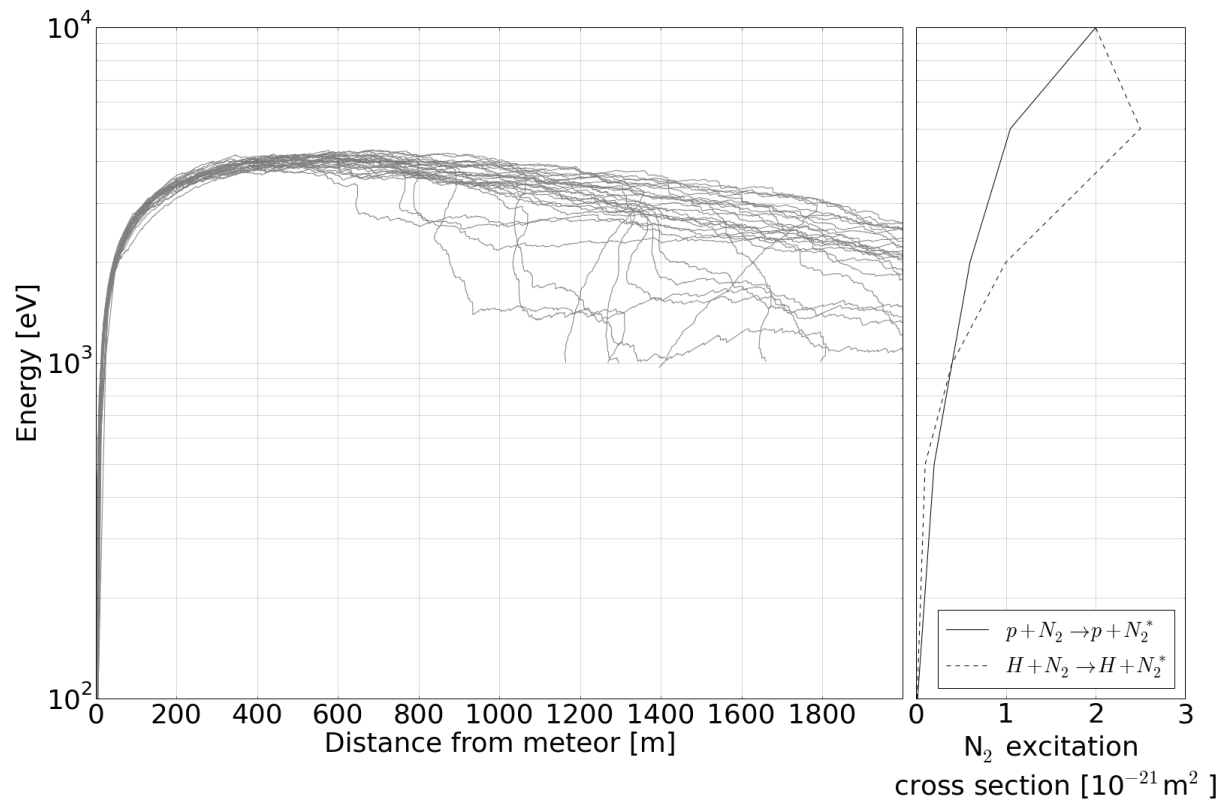


Figure S3: The energy of 30 randomly selected ejected particles relative to their distance from the meteor (left panel). The particles are followed until their energy drops below 1keV or their distance from the meteor exceeds 10 km. The right panel shows the energy dependence of the nitrogen excitation cross section responsible for the light production in our model.

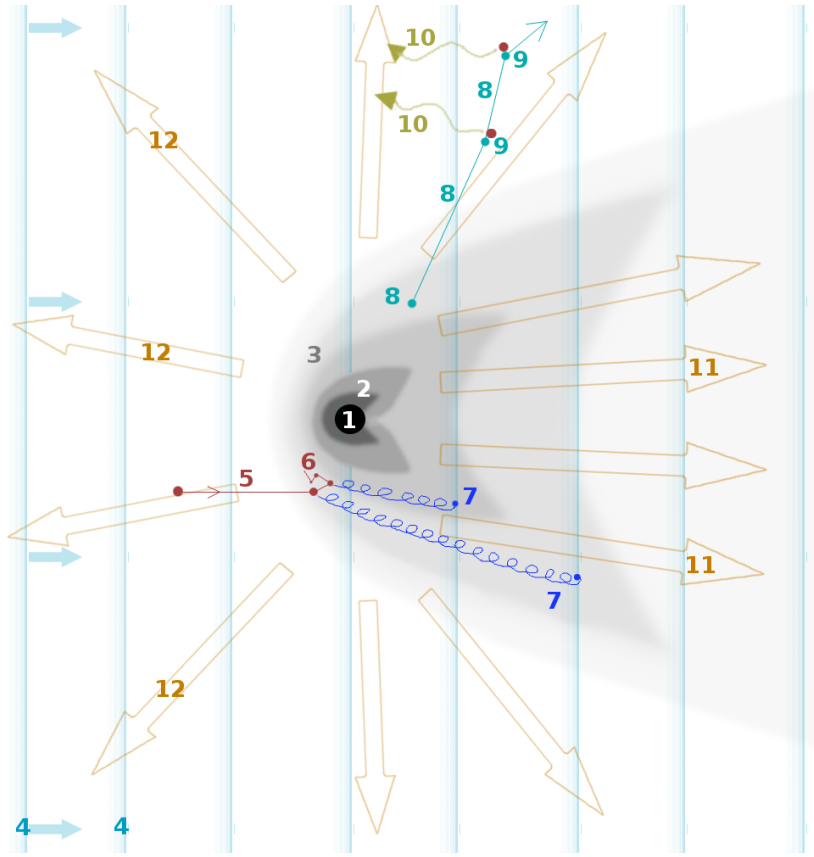


Figure S4: A simplified sketch of the processes used in our meteor charging model, shown from the reference point of a flying meteoroid [1]. The immediate vicinity of the meteoroid has the highest plasma density [2], while the diffuse shock region [3] has a lower density that smoothly connects to the surrounding ionosphere. The magnetic field [4] moves toward the meteor with the meteor speed, together with the atmospheric particles [5] that hit the meteor plasma [6]. The dynamics of ions created in such collisions is dictated by thermal collisions and ions stay coupled to the local meteor plasma [6]. Electrons from these collisions [7] have their collision frequency smaller than the electron cyclotron frequency, which means they start to gyrate and get trapped by the moving magnetic field. This creates a charge separation between ions and electrons, which results in an electric field within the meteor (and its wake) [11] and an electric field around the meteor head [12]. Electron gyration is not entirely free - electrons still experience some collisions. This enables the electric field [11] to reach its maximum when the electron drift reaches its steady state and further charge separation is stopped. Protons that appear in the meteor plasma [8] (mostly as a product of meteoroid ablation) get accelerated by the electric field and travel long distances [8], slowed down by collisions with the atmospheric species [9]. We are interested in collisions that excite N_2 molecules and create photons [10] detectable by the camera system used in the Leonid halo detection (2).

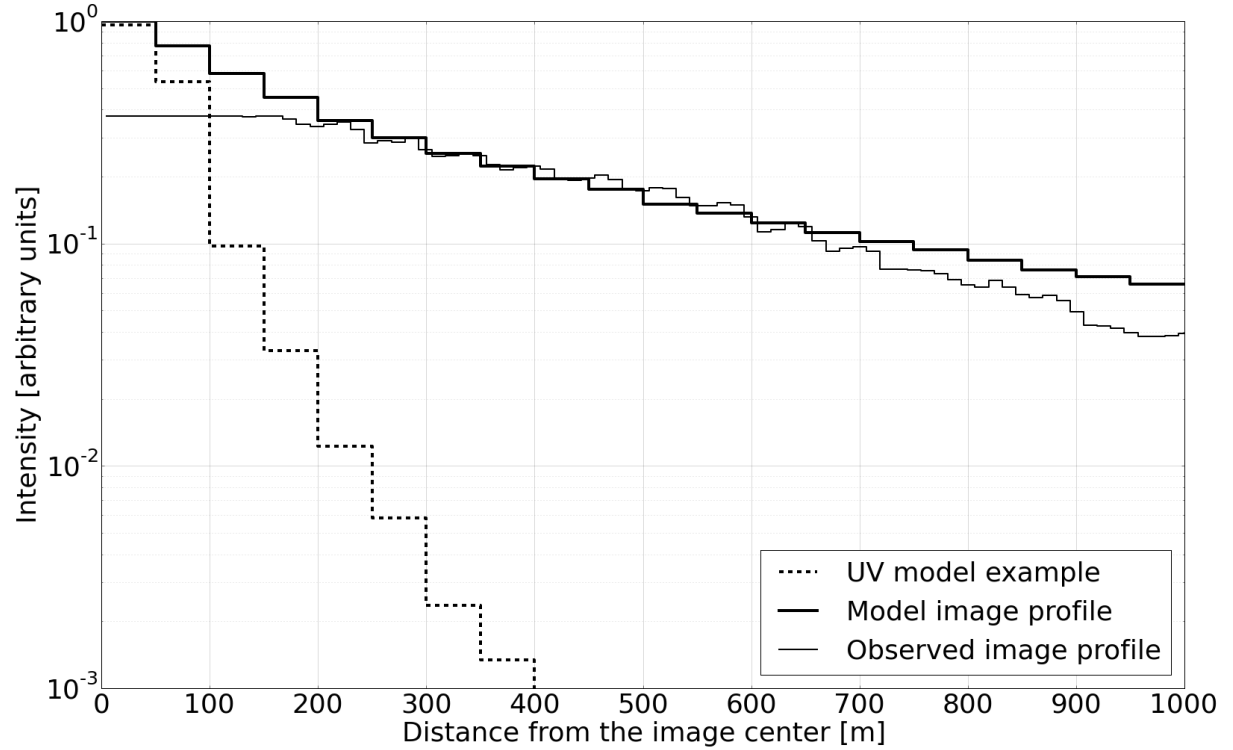


Figure S5: The intensity profile of the halo model image from the view of the camera (thick solid line). The cut off is taken from the image center along the direction perpendicular to the meteor flight. We show how it compares with the observed image profile (thin solid line) taken from Figure 1 in (2) (from the frame at 104.8 km altitude). The flat part of the observed intensity profile at distances $\lesssim 200$ m is due to pixel saturation and comparison with the model is not possible in that region. Brightness oscillations on the scale of ~ 50 m are artifacts of pixel size. For comparison we also show a typical intensity profile for a UV model of meteor halo with immediate photon emission (dotted line), which emphasizes the inability of precursor UV radiation to explain the size of the halo.

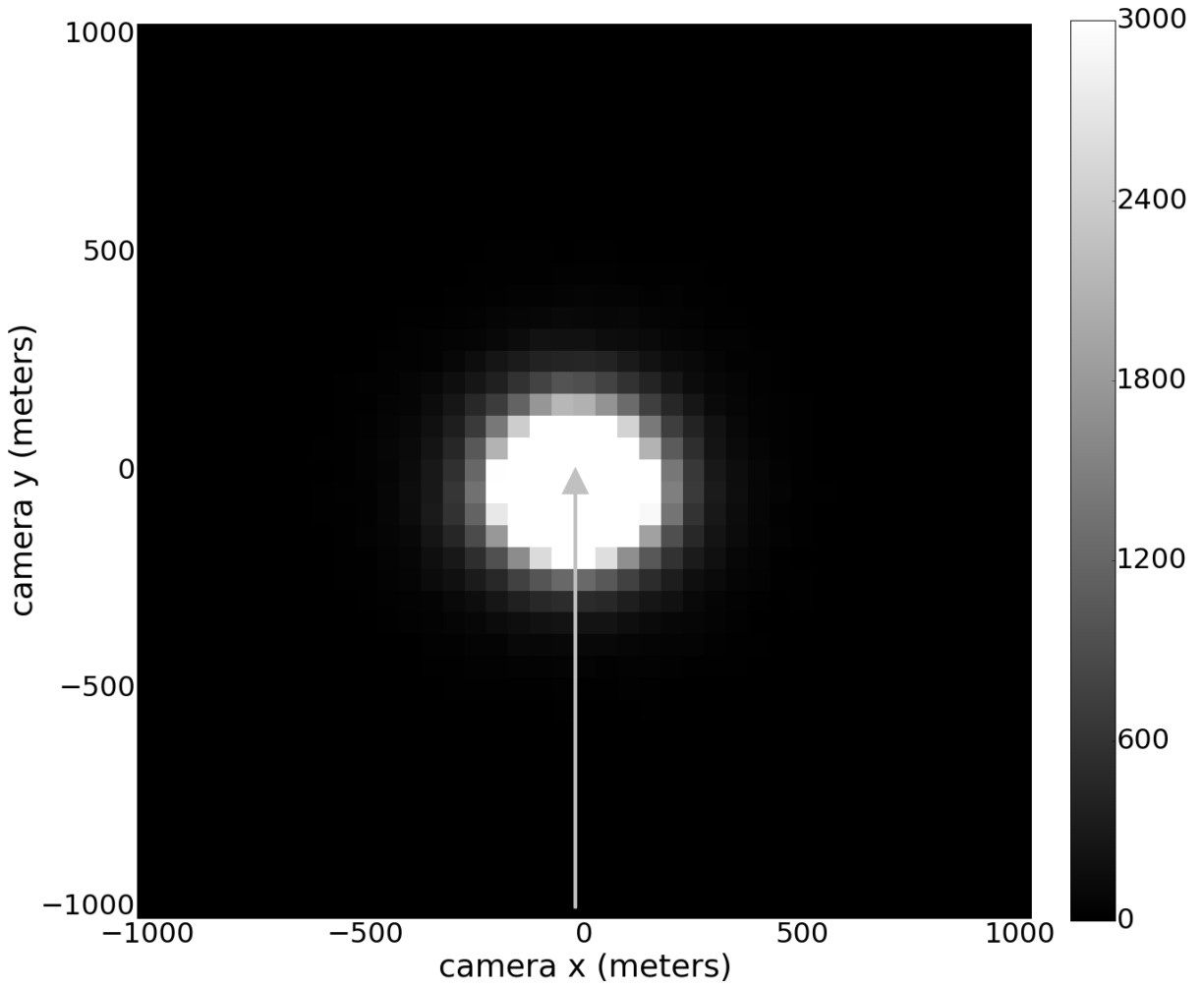


Figure S6: A simulated halo image using the model of UV photon absorption under the assumption of immediate emission of visible photons. The brightness level is adjusted to give saturated pixels up to about 200 m from the meteor center to match the observed image. The model intensity drops so fast with distance that there is no detectable halo brightness at larger distances from the meteor, hence excluding UV excitation as the source of halo brightness. The model used 1 million UV photons emitted along directions from 0° to 120° relative to the meteor direction.

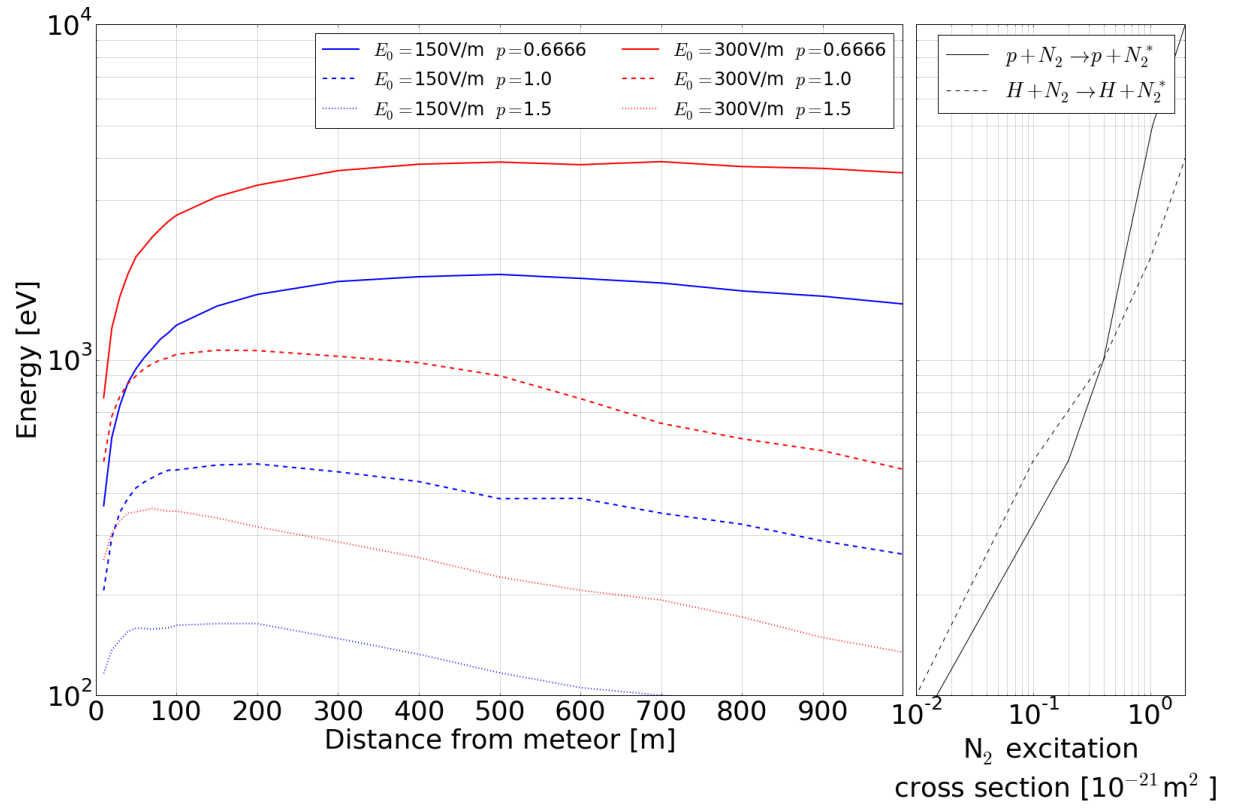


Figure S7: The energy of particles ejected under different electric fields (left panel). Each line is a median of energies of 30 randomly ejected particles accelerated by the electric field $E(r) = E_0/(r/r_0)^p$, where r is the distance from the meteoroid and $r_0 = 1$ m. The right panel shows the energy dependence of the nitrogen excitation cross section responsible for the light production in our model.

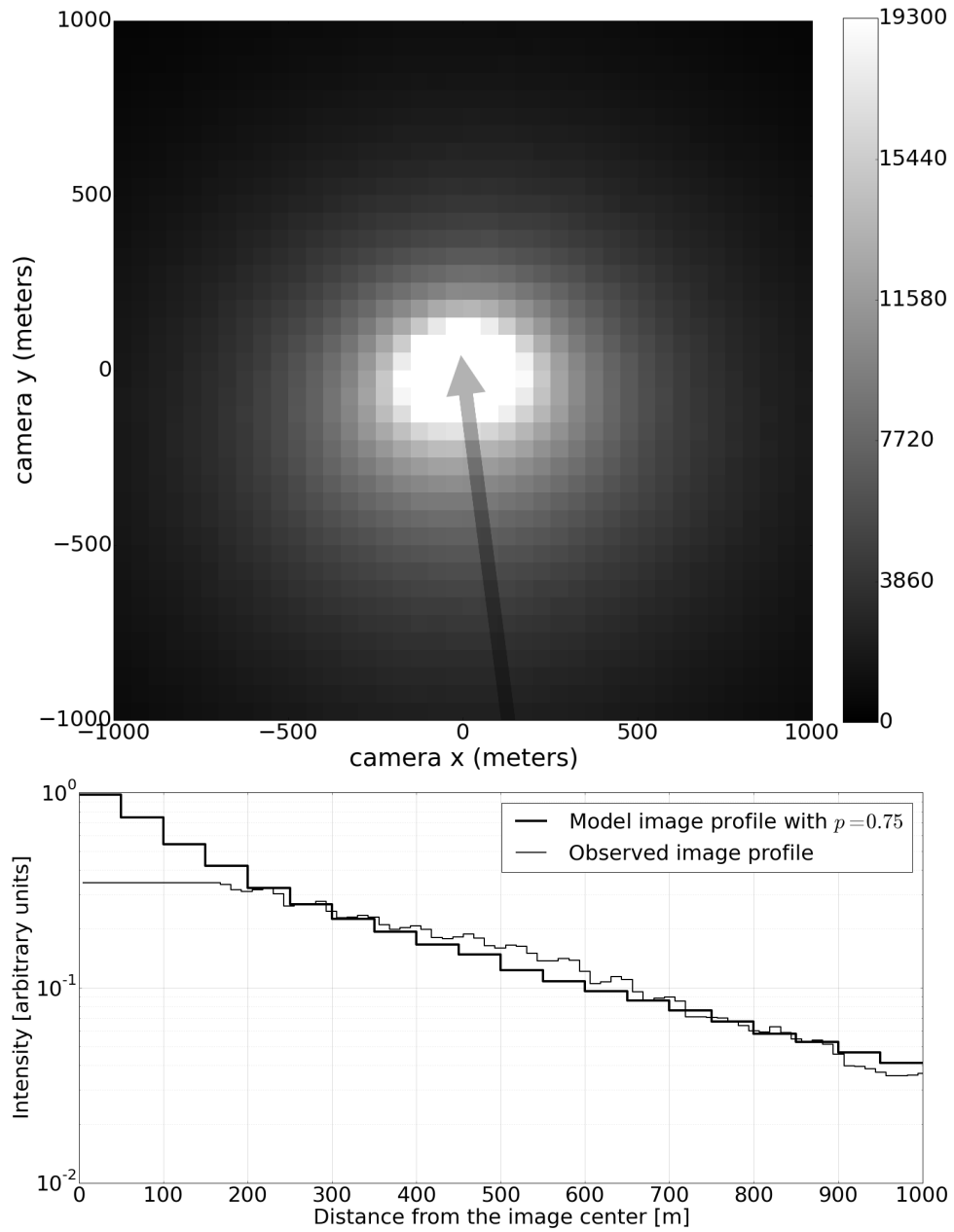


Figure S8: The simulated halo image and the intensity profile using a model where the electric field follows the $p = 0.75$ power law. An improvement is visible in matching the modeled and measured brightness profiles compared to the canonical model in figure S5.

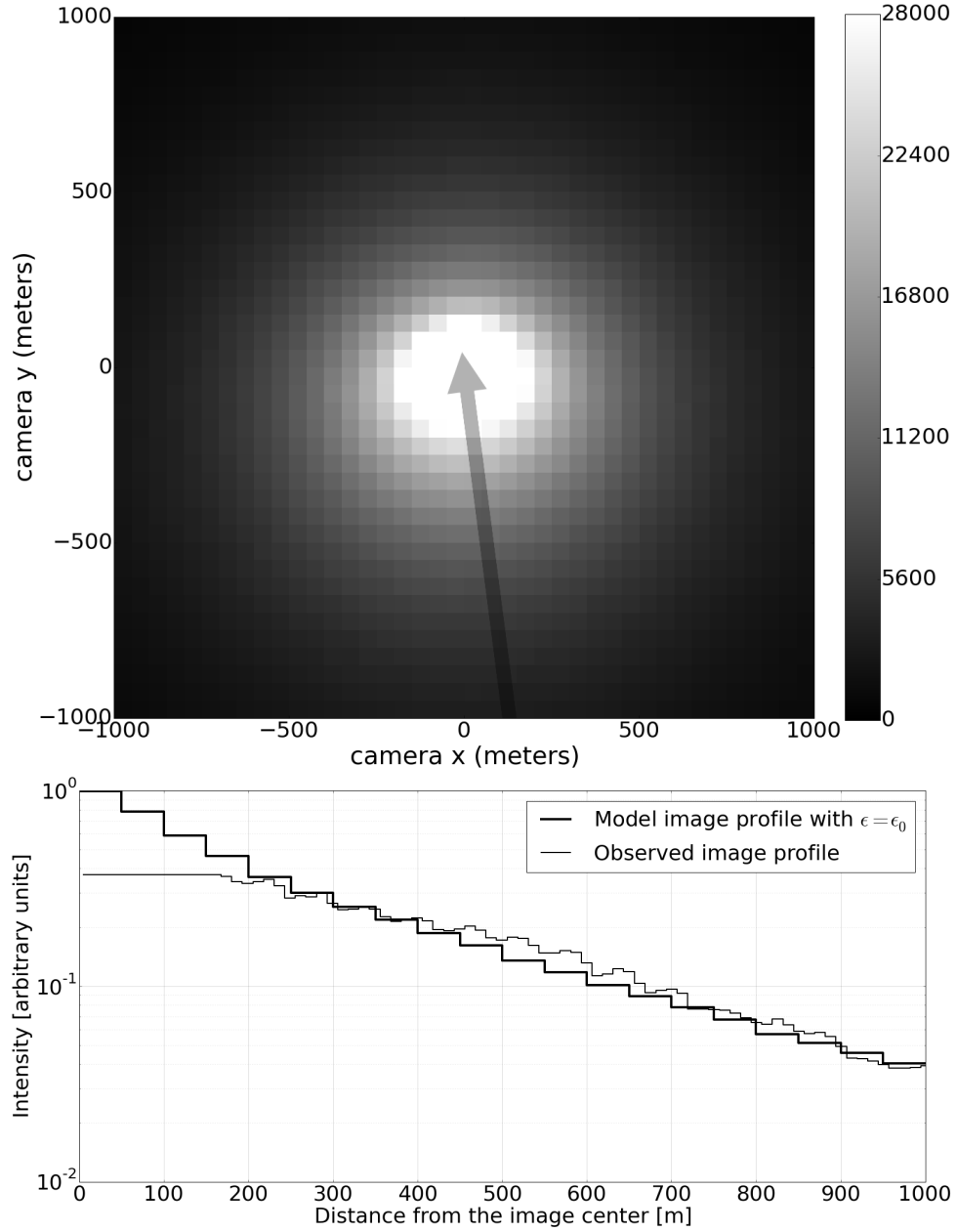


Figure S9: The simulated halo image and the intensity profile using a model where the scattering parameter is a constant $\epsilon = \epsilon_0$ (see equation 10). An improvement is visible in matching the modeled and measured brightness profiles compared to the canonical model in figure S5.